Applied Surface Science 573 (2022) 151529

Contents lists available at ScienceDirect

Applied Surface Science

journal homepage: www.elsevier.com/locate/apsusc

Full Length Article

Hydrogen permeation behavior and mechanism of multi-layered graphene coatings and mitigation of hydrogen embrittlement of pipe steel

Kejun Shi [a], Shu Xiao [a,b,*], Qingdong Ruan [b], Hao Wu [a], Guohua Chen [a], Chilou Zhou [a], Saihua Jiang [a], Ke Xi [a], Mohan He [a], Paul K. Chu [b,**]

[a] Institute of Safety Science & Engineering, South China University of Technology, Guangzhou 510641, China
[b] Department of Physics, Department of Materials Science and Engineering, and Department of Biomedical Engineering, City University of Hong Kong, Tat Chee Avenue, Kowloon, Hong Kong, China

ARTICLE INFO

Keywords:
Graphene
Hydrogen permeation barrier
Corrosion resistance
Molecular dynamics
Coatings

ABSTRACT

A method for *in situ* deposition of multi-layered graphene (MLG) coatings is demonstrated to mitigate hydrogen embrittlement of the X70 pipe steel. Carbon is implanted into the nickel catalytic layer pre-deposited by electroplating on the surface of the pipe steel, followed by annealing to segregate and form MLG. The MLG coatings are investigated systematically with respect to the surface morphology, phase structure, hydrogen resistance, corrosion resistance, and molecular dynamics simulation. In the stacked MLG structure, the *in situ* grown graphene layers interpenetrate each other to boost the coating adhesion and hydrogen resistance. Diffusion and the solid solution formed between the Ni coating and substrate improve the adhesion strength after annealing. The diffusion coefficient and permeability are reduced by 123 times and 48 times, respectively. Slow strain rate tests demonstrate outstanding resistance against hydrogen embrittlement because the MLG coatings inhibit hydrogen evolution, extend the diffusion path, decrease the permeation area, and enhance hydrogen adsorption. Moreover, electrochemical tests indicate that the MLG coatings have better corrosion resistance. These results reveal a viable strategy to use graphene to protect commercial steels from hydrogen embrittlement.

1. Introduction

Hydrogen energy is playing an increasingly significant role in the modern society because of its high calorific value and environmental friendliness.[1] Hydrogen transportation is an important part of hydrogen energy utilization, in which blending hydrogen with natural gas is a feasible large-scale energy transportation mode, [2] thus safe transportation to end users is critical. Transportation of hydrogen through steel pipes inevitably leads to hydrogen embrittlement (HE) because hydrogen penetration affects the microstructure, reduces the mechanical properties such as the tensile strength and fatigue strength, and eventually leads to brittle fracture, which can cause catastrophic and hazardous failures in the field. In order to reduce the thickness of the pipe wall, high strength steels are preferred, but higher strength is often accompanied by increased risk of hydrogen embrittlement. [3] Therefore, it is imperative to prevent or delay hydrogen permeation into pipe steels by means of hydrogen barrier coatings which can preserve the favorable bulk attributes of the steel materials. [4]

Although ceramic coatings such as SiC [5], Al_2O_3 [6,7], Er_2O_3 [8,9], and so on have good hydrogen resistance, they are brittle and therefore, cracking and spalling caused by the difference in the thermal expansion coefficients between the coating and substrate can lead to failure in the field, especially under harsh conditions. Application of graphene and other two-dimensional materials to hydrogen resistant coatings has recently attracted research interests, which has low permeability, high thermal stability, remain chemically inert, and remain mechanically robust. [10,11] Graphene has unique two-dimensional characteristics and studies have shown that the perfect graphene sheet is impermeable to standard gases. [12,13] First-principles calculation demonstrates that the dense electron cloud of the six-member ring network exhibits excellent barrier characteristics to micro-particles and even hydrogen. [14] The hydrogen is expected to take billions of years to penetrate graphene's dense electronic cloud. [15] However, the impermeability of defect-free graphene to hydrogen has been recently contested since

* Corresponding author at: Institute of Safety Science & Engineering, South China University of Technology, Guangzhou 510641, China.
** Corresponding author.
E-mail addresses: xiaos@scut.edu.cn (S. Xiao), paul.chu@cityu.edu.hk (P.K. Chu).

https://doi.org/10.1016/j.apsusc.2021.151529
Received 31 August 2021; Received in revised form 4 October 2021; Accepted 4 October 2021
Available online 19 October 2021

Table 1
Alkaline pyrophosphate bath system.

Composition	Concentration
$NiSO_4{\cdot}6H_2O$	0.3 mol/L
$Na_4P_2O_7{\cdot}10H_2O$	0.75 mol/L
$C_6H_8O_7{\cdot}H_2O$	0.12 mol/L

experimental evidence. Ripples, wrinkles and other defects inducing a local curvature are catalytically active and allow non-negligible permeation of hydrogen. [16] The flipping of a chemisorbed atomic hydrogen from one side to the other of a graphene layer is highly dependent on the local density of the chemisorbed hydrogen atoms on the 2D carbon surface, while the transmission of atomic hydrogen becomes competitive for a high saturation of a given graphene ring. [17] Even though, graphene is still a potential hydrogen barrier material. Young et al. [18] have shown a reduction in deuterium permeation by a factor of ~28 compared to copper alone, indicating an impressive reduction for an atomically thin material. Nam et al. [19] have demonstrated that a graphene coating can reduce hydrogen embrittlement of copper according to slow strain rate tensile tests. Fan et al. [20] have shown that the graphene coating reduces the hydrogen permeability into nickel by 50%, and the limited hydrogen resistance is mainly due to the gap between graphene grains, which creates conditions for hydrogen diffusion. Other studies have shown that graphene can be prepared *in situ* on Ni, Cu, and other metal substrates [21–26], but *in situ* growth of graphene on steels and subsequent improvement in hydrogen resistance have not been investigated systematically. It is obviously impractical to use the traditional spin coating method to deposit graphene onto the inner surface of steel pipes. Zhou et al.[27] have prepared the Ni-graphene composite coating on QP steel by reverse pulse electrodeposition, but the effects on hydrogen resistance are limited, because the co-deposition method cannot produce the perfect graphene coating on the substrate. Therefore, a practical and effective technique to deposit graphene coatings on pipeline steel *in situ* is crucial to improving the hydrogen resistance.

In this study, a multi-layered graphene (MLG) coating is designed and fabricated on the X70 pipe steel *in situ* and the structure, hydrogen

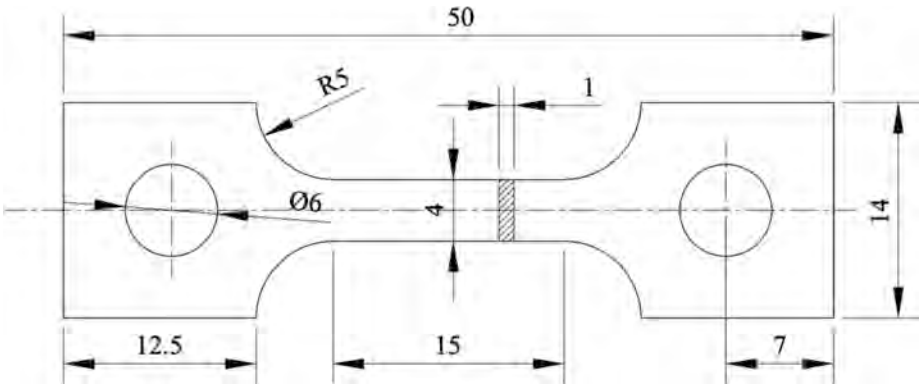

Fig. 1. Schematic diagram of the tensile specimen. (Unit: mm).

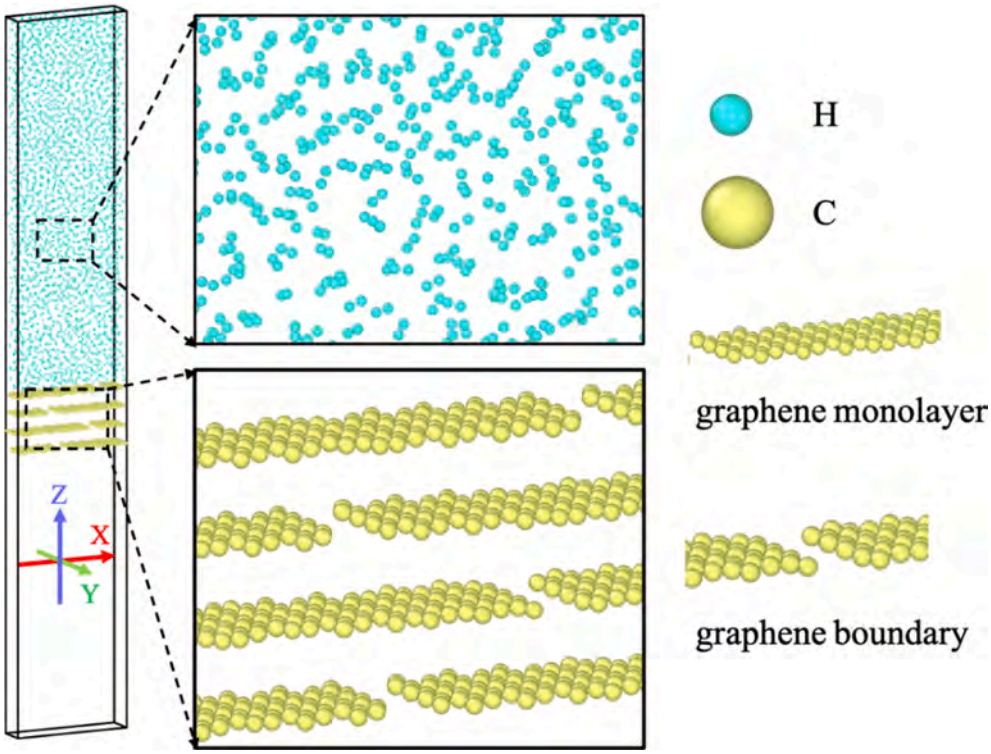

Fig. 2. Molecular dynamics model of the hydrogen barrier process of MLG.

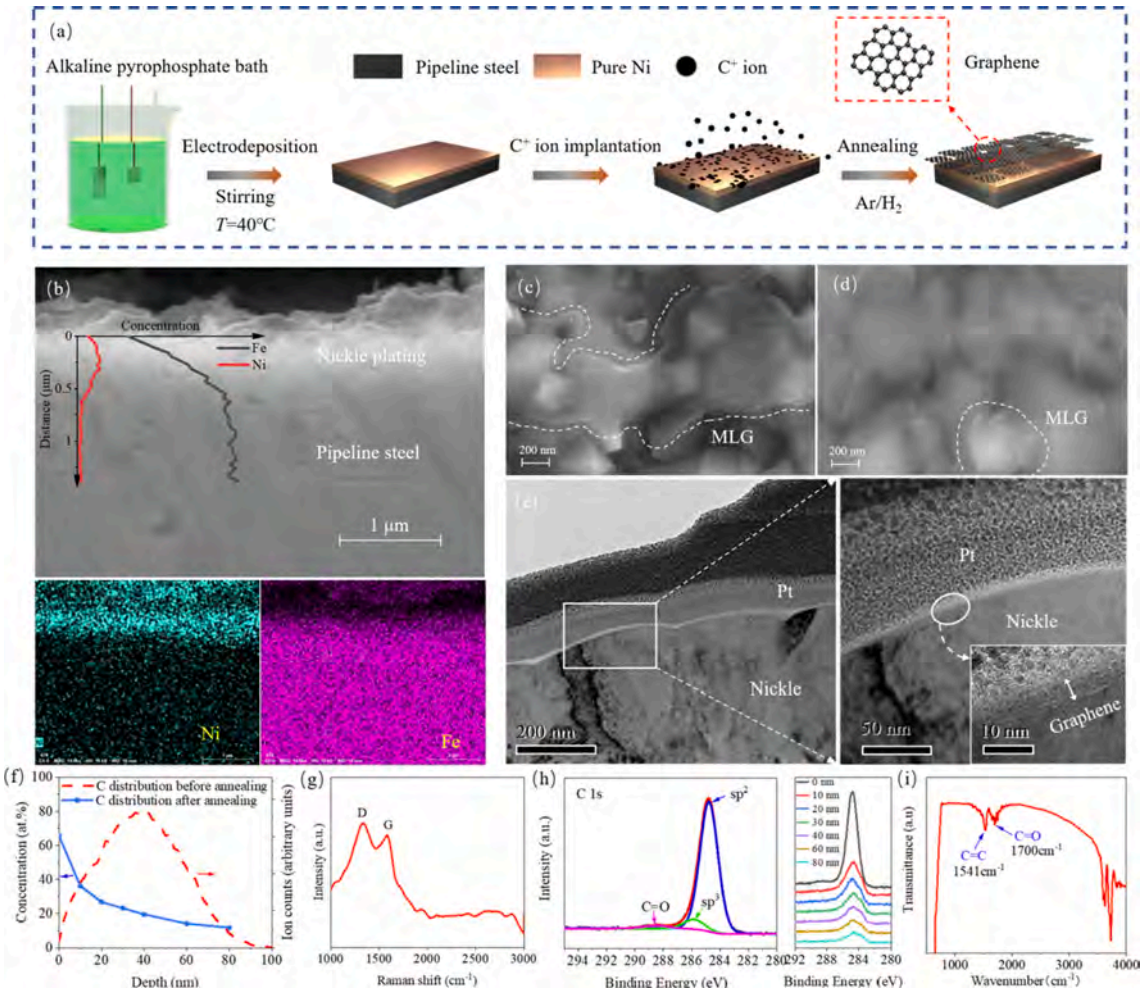

Fig. 3. Fabrication and characterization of multi-layered graphene: (a) Schematic of the MLG coating fabrication process; (b) SEM and EDS images of the cross-sectional structure of the nickel plate; (c, d) Planar SEM images and (e) Cross-sectional TEM images of MLG; (f) C distribution before and after annealing; (g) Raman scattering spectrum, (h) XPS spectra, and (i) FTIR spectrum of MLG.

resistance, and corrosion resistance are investigated systematically. In this technique, a nickel catalytic layer is prepared on the steel substrate electrochemically and the MLG coating is formed by C ion implantation and annealing. The surface effects of the coating are determined based on the hydrogen evolution kinetics and the hydrogen resistance mechanism is analyzed by molecular dynamics simulation. Compared with previous studies only focusing on whether hydrogen atoms can pass through the six-member ring of graphene, our study simulates and analyzes the process in which hydrogen passes through multilayered graphene with defects and the corrosion resistance is assessed by electrochemical measurements.

2. Materials and methods

2.1. In situ fabrication of multi-layered graphene (MLG) coatings

The X70 pipe steel substrate was cut into 50 mm × 30 mm × 1 mm rectangular pieces by wire cutting, polished with sandpaper to a mirror finish, cleaned with acetone and ethanol ultrasonically, and dried. The analytical grade chemicals were purchased from Aladdin and used without purification. A 99.99% pure graphite target was used as the source in ion implantation.

A nickel catalytic layer was pre-deposited on the X70 substrate by electrodeposition in which an alkaline sodium pyrophosphate bath system (Table 1) with a pH of 9.5 was utilized. The steel substrate was the working electrode, whereas the SCE and platinum plate were the reference electrode and counter electrode respectively. Electrodeposition was carried out using a current density of 20 mA/cm^2 for 1 h at 40 °C. Afterwards, C was ion implanted into the nickel layer using a MEVVA source. The implantation voltage and dose were 30 keV and 2.4 × 10^{16} ions/cm^2 (6 MG, equivalent to six layers of graphene), respectively. After ion implantation, the sample was annealed at 700 °C for 1 h and then cooled at a rate of 20 °C/min. Before annealing, the furnace tube was evacuated and a mixture of H_2 and Ar was bled into the furnace continuously to cover the sample.

2.2. Electrochemical hydrogen permeation evaluation

The electrochemical hydrogen permeation test was carried out using the Devanathan-Stachurski (D-S) cell[27] composed of the cathode cell (hydrogen charging), anode cell (hydrogen detecting) with a platinum plate being the counter electrode, SCE as the reference electrode, and sample as the working electrode. The cathode cell was filled with a 0.2 mol/L NaOH containing 3 g/L NH_4SCN. By applying a constant current, hydrogen evolution occurred on the surface of the sample and the generated hydrogen diffused to the other side of the sample. The cathode cell was filled with 0.2 mol/L NaOH and when a positive voltage was applied to the anode side, the permeated hydrogen was oxidized to H^+ and the electrical signal was monitored by the electrochemical workstation to assess hydrogen permeation. Before the test, the background

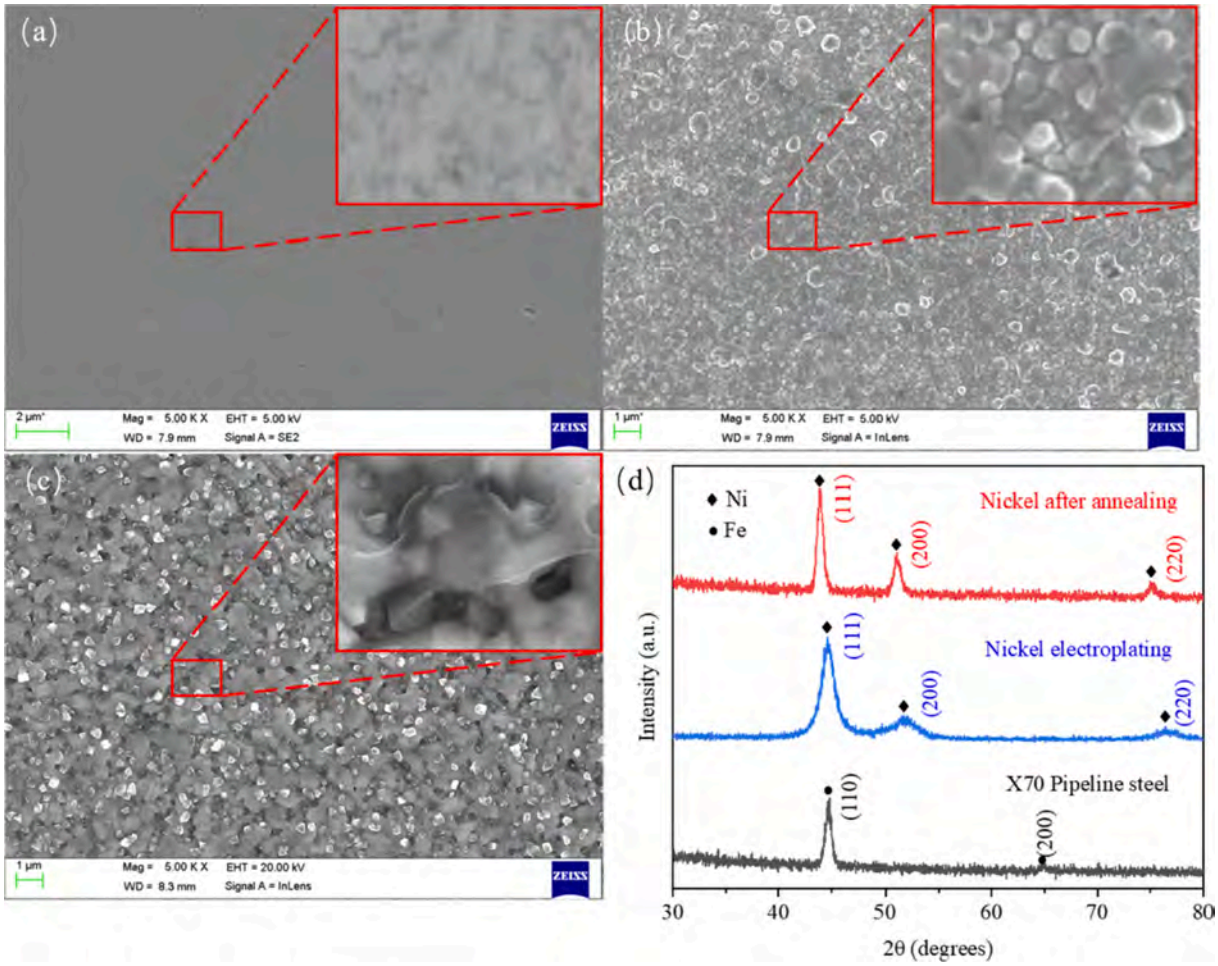

Fig. 4. Surface morphology: (a) Nickel coating before annealing, (b) Nickel coating after annealing, and (c) MLG coating; (d) XRD patterns of the nickel coating before and after annealing.

current was reduced to less than 0.1 μA/cm^2 by imposing a constant potential of 200 mV (vs. SCE) in the anodic cell and then a constant current of −12 mA/cm^2 was applied to the cathode to start the test. The apparent diffusion coefficient of hydrogen D_{app} and permeability J were obtained from the permeation curve by the following equations [28]:

$$D_{app} = L^2/15.3t\text{and} \quad (1)$$

$$J = i_p^{\infty} \times L/F \quad (2)$$

where L is the thickness of the sample, cm; t is breakthrough time, s; i_p^{∞} is the steady-state current density, μA/cm^2; F = 96,485 C/mol.

2.3. Slow strain rate test

The slow strain rate test (SSRT) was employed to evaluate the resistance to hydrogen embrittlement (HE).[29] The mechanical properties of the samples before and after hydrogen charging were measured by SSRT and the susceptibility of the sample to HE was assessed. The samples were processed into non-standard tensile samples as shown in Fig. 1 with a parallel length of 15 mm, gauge width of 4 mm, and thickness of 1 mm. The hydrogen charged samples were pre-charged electrochemically at 50 mA/cm^2 for 24 h before SSRT. After hydrogen charging, the test was conducted immediately to avoid thermal desorption and escape of hydrogen. The strain rate was 5.5×10^{-5} /s. Except for the gauge section on the coating side, the samples coated with MLG were covered with sealing mud, so that hydrogen charging only occurred on the coating surface of the gauge section. The uncoated samples were also charged on one side to ensure the same exposure area as the coated samples.

2.4. Electrochemical measurements

Electrochemical impedance spectroscopy (EIS) and potentiodynamic polarization were employed to analyze the corrosion characteristics of the samples immersed in 3.5 wt% NaCl for 1 h. The tests were conducted using a three-electrode electrochemical workstation (Reference 600+, Gamry, America) with an exposed surface area of 1 cm^2 on the working electrode, while the SCE and platinum plate were the reference and counter electrodes. Potentiodynamic polarization was conducted at a scanning rate of 1 mV/s in the potential range from −0.5 V (vs. OCP) to + 0.5 V (vs. OCP). EIS was carried out at the open-circuit potential (OCP) and the frequencies ranged from 100,000 Hz to 0.1 Hz with a perturbation potential of 20 mV.

The cathodic polarization curves were obtained by linear sweep voltammetry (LSV) to analyze the hydrogen evolution kinetics. The electrolyte was 0.2 mol/L NaOH. The sample served as the working electrode, SCE was the reference electrode, and platinum plate was the counter electrode. The scanning rate was 1 mV/s from 0 V (vs. OCP) to −1.5 V (vs. OCP).

2.5. Characterization

The morphology of the samples was examined by field-emission scanning electron microscopy (SEM, Merlin, Zeiss) and transmission

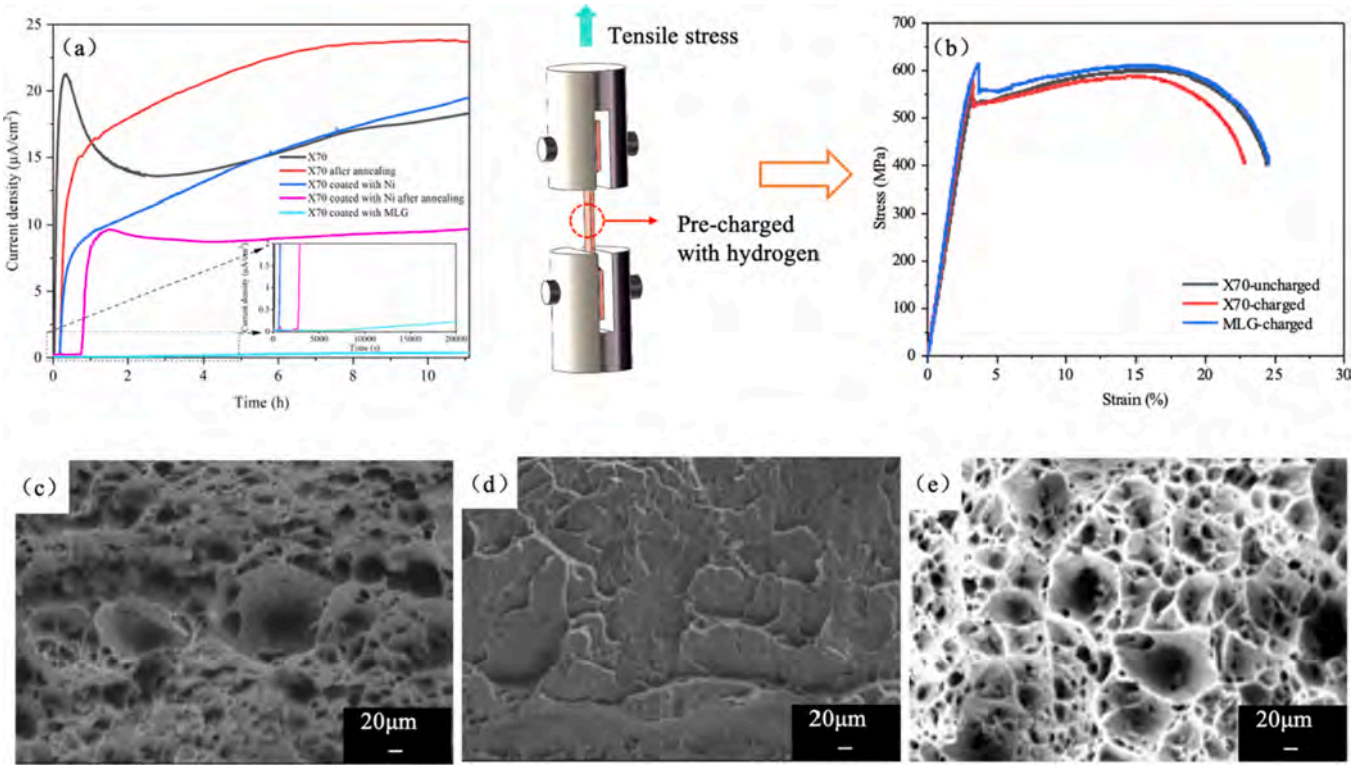

Fig. 5. (a) Electrochemical hydrogen permeation curves; (b) Strain-stress curves of the uncoated and coated samples after electrochemical hydrogen charging; Fracture morphologies of (c) X70 after annealing without hydrogen charging, (d) X70 after annealing with hydrogen charging, (e) MLG with hydrogen charging.

Table 2
Hydrogen permeation parameters of the different samples.

Samples	t_b (s)	$I_{t=40000s}$ ($\mu A \cdot cm^{-2}$)	D_{app} ($cm^2 \cdot s^{-1}$)	J ($mol \cdot (cm \cdot s)^{-1}$)
X70	80	18.37	8.17×10^{-6}	1.90×10^{-5}
X70 after annealing	670	21.73	9.76×10^{-7}	2.25×10^{-5}
X70 coated with Ni	580	19.5	1.13×10^{-6}	2.02×10^{-5}
X70 coated with Ni after annealing	2700	9.50	2.4×10^{-7}	9.85×10^{-6}
X70 coated with MLG	9830	0.38	6.65×10^{-8}	3.94×10^{-7}

electron microscopy (TEM, JEM-3200FS, JEOL). The elemental distribution was determined by energy-dispersive X-ray spectroscopy (EDS). The chemical composition and structure were analyzed by Raman scattering (LabRAM HR, Horiba), X-ray photoelectron spectroscopy (XPS, ESCALAB 250X, Thermo Fisher), as well as Fourier transform infrared spectroscopy (FTIR, Nicolet IS50, Thermo Fisher). The microstructure was characterized by X-ray diffraction (XRD, Smartlab, Rigaku).

2.6. Molecular dynamics (MD) simulation

The simulations were conducted using the numerical package LAMMPS [30] and the adaptive intermolecular reactive empirical bond order (AIREBO) model [31] was adopted in the MD simulation. The periodic boundary conditions in all three directions were applied to the × and y axis, while the z axis was fixed. The time step was 0.5 fs and the MD calculation was performed at T = 300 K controlled by a Nosé–Hoover thermostat, which emulated the canonical NVT ensemble corresponding to the constant number of atoms N, constant volume V, and constant temperature T. The model is presented in Fig. 2.

3. Results and discussion

3.1. Fabrication and characterization

As shown in Fig. 3(a), *in situ* fabrication of the MLG coating on the X70 steel substrate includes three key steps. Firstly, a Ni catalytic layer is pre-deposited on the pipeline steel by electrochemical deposition. Secondly, C ions are implanted into the Ni catalytic layer and thirdly, the sample is annealed to facilitate segregation and nucleation. The last step not only forms graphene *in situ*, but also accelerates Ni diffusion to the substrate to form a solid solution. As shown in Fig. 3(b), the interface between the Ni layer and substrate disappears, while a Ni diffusion layer is formed after annealing, thereby confirming the graded distribution of Ni in this region, which is expected to improve the adhesion strength of the coating.

Fig. 3(c) depicts the morphology of MLG and Fig. 3(d) shows that MLG encapsulates the protruding grains one by one, indicating that MLG has good coverage to retain the original shape. As shown in Fig. 3(e), the layered structure of MLG is examined by TEM. MLG nucleates *in situ* on the surface of Ni and grows epitaxially along the surface of Ni grains until the substrate is fully covered. The good coverage provides the favorable conditions for hydrogen resistance. MLG is covalently bonded with the Ni layer, which has a higher binding energy than physical adsorption [32] so as to mitigate coating failure in the field. From Fig. 3 (e), the thickness of MLG is 4 nm (6 layers approximately) and the layer spacing is slightly larger than the theoretical thickness of single-layer graphene (0.34 nm) due to the existence of oxygen-containing functional groups. The implantation dose of C is 6 MG and so MLG is composed of 6 layers after the implanted C ions segregate. However, the thickness of MLG on the surface is not uniform and in some areas is less than 6 layers. This is because the segregation process of C is not complete, and some C ions remain in the nickel layer or diffuse to the substrate, resulting in the reduction of C segregation. In addition, the migration of carbon ions after annealing forms an uneven distribution,

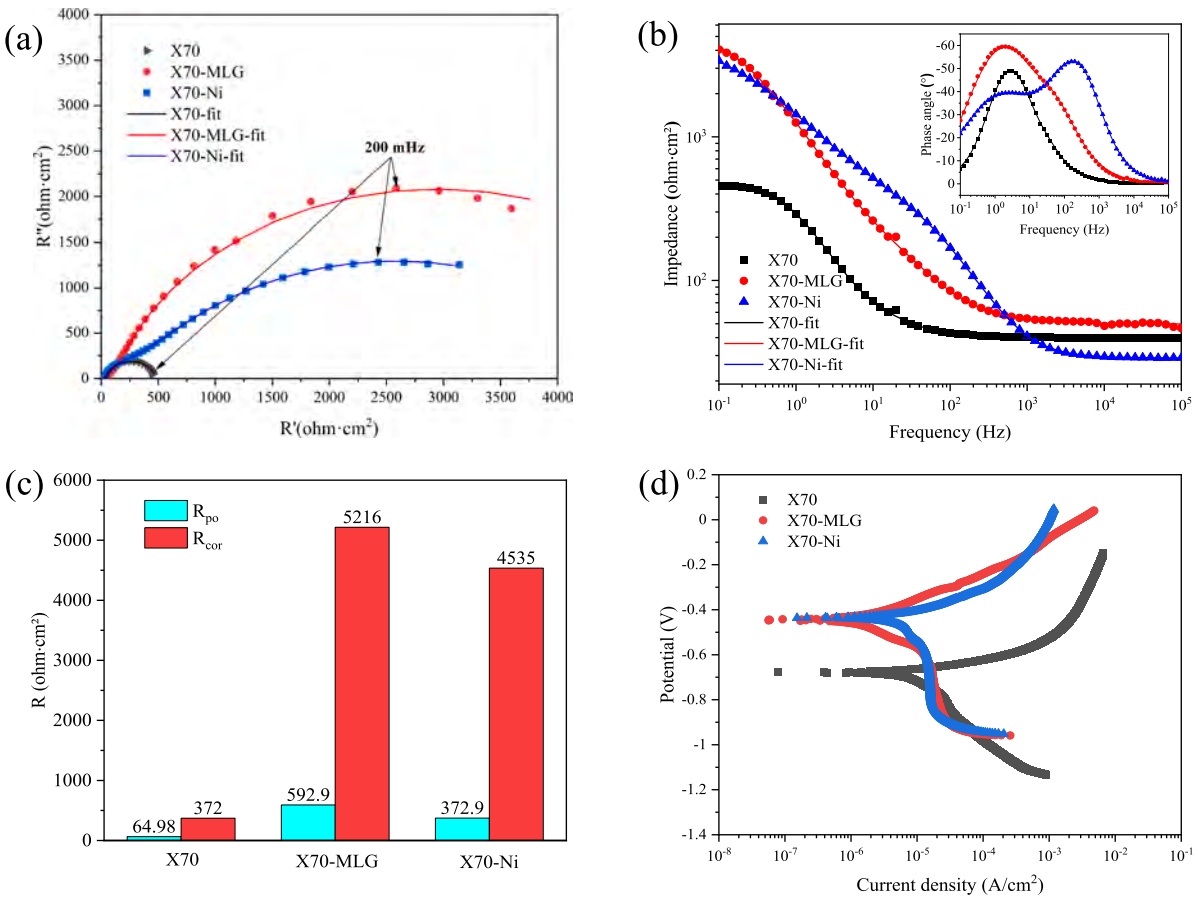

Fig. 6. Corrosion properties: (a) Nyquist plots. (b) Impedance and phase angles; (c) Charge transfer resistance (R_{cor}) fitted by EIS; (d) Tafel curves.

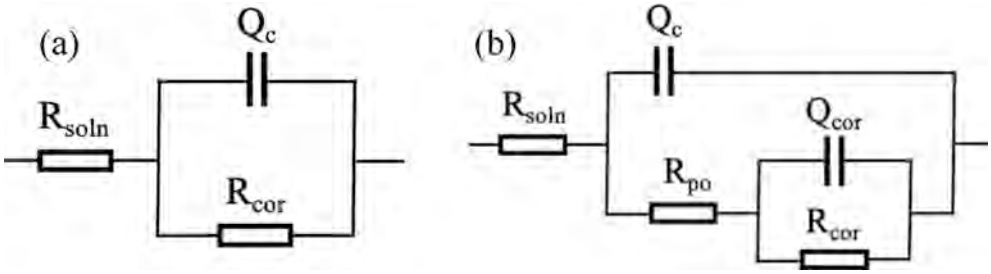

Fig. 7. Equivalent circuit models: (a) Bare steel and (b) Coated steel.

Table 3
Corrosion parameters derived from the Tafel curves.

Samples	E_{cor} (V)	I_{cor} (μA/cm^2)
X70	−0.681	5.6
X70-MLG	−0.447	1.2
X70-Ni	−0.442	5.2

and the final number of nucleation layers is affected by the morphology of nucleation position.

Fig. 3(f) shows diffusion and migration of C after annealing. The distribution of C in the Ni layer before annealing is simulated by SRIM. The C profiles exhibits a Gaussian distribution and XPS shows that most of the C ions segregate to the surface and the C concentration decreases with depth, indicating that segregation is not complete. In the annealing process, the implanted C ions are activated and diffuse leading to segregation as the solubility decreases when the temperature drops. The boundary curvature radius of the Ni grains affects segregation and nucleation of graphene at the grain boundary. [33] Graphene nucleates on the atomic steps of the Ni grain boundary and then graphene layers grow on several steps form MLG. Therefore, the larger the Ni grain, the larger is the radius of curvature, the fewer atomic steps, the fewer graphene layers are formed. The surface of Ni deposited by electrochemical deposition is rough and the grain size is different. Hence, the number of graphene layers is also different. In addition to nucleation of graphene, C ions segregated near the graphene nuclei are attached to the edge of graphene lattice leading to 2D epitaxial growth along the Ni crystal surface to form the coating with an uneven grain surface.

As shown by the Raman scattering (Fig. 3(g)), the intensity ratio (I_D/I_G) of the D band (1340 cm^{-1}) to G band (1586 cm^{-1}) is large thus reflecting a large defect density in MLG. The enhanced D band should be assigned to the edges of the nanometer sheets and the presence of stacking disorder in the sheets. [34] The XPS spectrum of MLG in Fig. 3 (h) shows two strong peaks at 284.78 eV and 285.83 eV related to sp^2

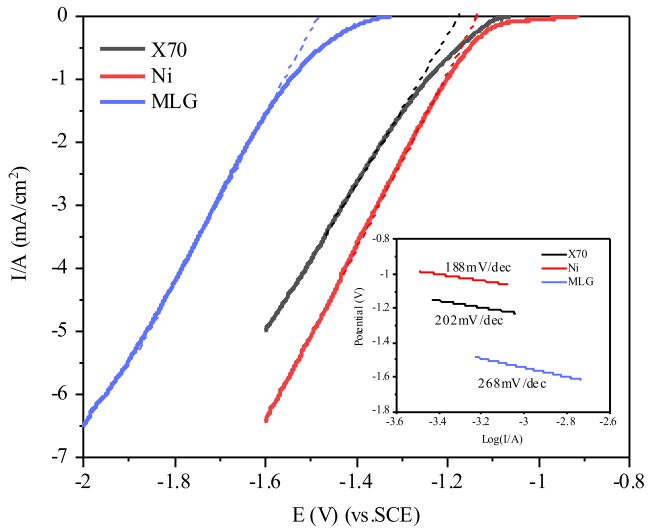

Fig. 8. Cathodic polarization curves and Tafel slopes.

Table 4
Hydrogen evolution kinetics and parameters.

Samples	E_e	E	η	$-b$
X70	−1.029 V	−1.175 V	0.146 V	202 mV/dec
Ni	−1.029 V	−1.136 V	0.107 V	188 mV/dec
MLG	−1.029 V	−1.484 V	0.455 V	268 mV/dec

hybridization and sp^3 hybridization [35], respectively. The surface C atoms are essentially sp^2. The weak peak at 288.54 eV arises from C═O indicating that oxygen-containing functional groups are incorporated in the growth process. There are two main sources of O atoms, from the environment arising from non-UHV conditions and pipeline steel substrate. After annealing, oxygen atoms diffuse to the surface of the nickel layer and bond with graphene. Owing to the high annealing temperature, most of the C—O functional groups are removed by thermal reduction leaving only a small amount of C═O bonds. The oxygen-containing functional groups introduce defects in graphene thus explaining the large I_D/I_G ratio in Fig. 3(g). Fig. 3(h) shows that the half-peak width of the main peak widens gradually with increasing etching depth and the proportion of sp^3 carbon increases gradually, indicating that the carbon structure tends to be disordered along the depth direction. The FTIR spectrum in Fig. 3(i) corroborates the formation of MLG. The peak at 1541 cm^{-1} represents C═C and that at 1700 cm^{-1} stems from C═O (carbonyl) consistent with XPS.

The surface morphologies of the Ni layer before and after annealing are shown in Fig. 4(a) and 4(b) respectively. Before annealing, the surface is smooth and uniform. After annealing, the surface shows a large number of spherical crystals and the roughness increases significantly. Fig. 4(c) shows the surface of the Ni layer is coated with MLG, which covers the uneven Ni layer and fills the gap between crystallites leaving very little exposed crystallites. Fig. 3(d) indicates that the exposed crystallites are actually wrapped by MLG. MLG exhibits macroscopic uniformity, continuity, and integrity. Fig. 4(d) displays the XRD patterns of the Ni layer before and after annealing. The Ni grains before and after annealing show the (111) plane mainly with a small amount of (200) and (220) crystal planes. The hexagonal lattice constants of Ni (111) and graphene are 2.497 Å and 2.46 Å respectively. There is a good lattice match between the two and so the Ni (111) plane can promote nucleation and growth of graphene. [36] The Ni (111) peak before annealing is relatively wide indicating that the Ni grains deposited by electrodeposition are relatively small, which is only approximately 1.2 nm. The grain size can be calculated by applying Scherrer formula from the diffraction peak of Ni. After annealing, the diffraction peak narrows and becomes sharper, and the grain size of Ni increase to about 6.5 nm, which is consistent with SEM. The larger Ni grain size is favorable to the formation of graphene with fewer layers and orderly stacking. In addition, the stress change caused by diffusion shifts the Ni peak offset to the left.

3.2. Hydrogen permeation

The electrochemical hydrogen permeation results are shown in Fig. 5 (a). The hydrogen steady-state current of the sample coated with MLG is much lower than that of the X70 pipeline steel and the hydrogen breakthrough time is prolonged significantly. However, the breakthrough time of the sample coated with the Ni coating or annealed is only slightly longer and the current reaches the steady state faster after annealing. The hydrogen permeation parameters calculated by Eqs. (1) and (2) are presented in Table 2.

The apparent hydrogen diffusion coefficient D_{app} of the MLG sample is 6.65×10^{-8} cm^2/s, which is 123 times less than that of the substrate and the hydrogen permeability J decreases by 48 times to 3.94×10^{-7} mol/(cm·s). The permeation current of the untreated X70 continues to rise, but the MLG sample reaches a steady state showing that the actual hydrogen barrier permeability is more than 48. Annealing does not reduce the hydrogen permeability of pipeline steel. The grain boundary is a fast channel for hydrogen diffusion and the amount of boundary decreases with larger grain size after annealing and therefore, D_{app} of X70 after annealing decreases. Meanwhile, the decrease of acicular ferrite reduces the dislocation density and hydrogen trapping to increase the hydrogen permeability. The effects of the pure Ni coating before annealing on hydrogen permeation are not appreciable only showing a small inhibition effect in the initial stage of hydrogen permeation. During the electrodeposition process of the Ni coating, bubbles appear from the surface leading to the formation of void defects and so it cannot be a good barrier. Due to the small grain size of nickel, there are a large number of grain boundaries for short-circuit diffusion. Hydrogen diffusion along some types of grain boundaries in Ni is at least two orders of magnitude faster compared to the bulk. [37] In the case of nanocrystalline nickel and despite a high density of traps, the mechanism of short-circuit diffusion dominates the trapping effect. After annealing, the apparent hydrogen diffusion coefficient D_{app} of the Ni coated sample decreases to 2.4×10^{-7} cm^2/s and the hydrogen permeability J decreases to 9.85×10^{-6} mol/(cm·s). As shown in Fig. 4, annealing greatly increases the grain size of nickel and reduces the grain boundary and defects, resulting in a significant decrease in the diffusion rate of hydrogen along the grain boundary. Oudriss et al. [38] showed that the permeability of polycrystalline nickel is almost one order of magnitude higher than that of single crystal nickel. In conclusion, the MLG coating has excellent hydrogen permeation resistance and significantly inhibits permeation and diffusion of hydrogen to the pipeline steel substrate.

The strain-stress curves of the uncoated and coated samples after electrochemical hydrogen charging are shown in Fig. 5(b). The yield strength and fracture strength of the X70 pipeline steel without charging are 526 MPa and 600 MPa respectively, and elongation is 19.6%. After hydrogen charging, the fracture strength and elongation of the uncoated sample decrease, indicating that hydrogen charging deteriorates mechanical properties of pipeline steel and reduces the plasticity. Long-term charging enriches hydrogen in the pipeline steel and forms hydrogen molecules. With the gradual increase of the hydrogen pressure, irreversible hydrogen damage such as microcracks appears, which eventually compromises the mechanical properties. The mechanical properties of the sample coated with MLG don't decrease after charging and the original plasticity is maintained, showing that the MLG coating prevents diffusion of hydrogen into the pipeline steel substrate during charging resulting in good hydrogen embrittlement resistance. The tensile fracture morphology is shown in Fig. 3(c–e). The fractured annealed X70 pipeline steel without charging shows the typical dimple morphology and the dimple size is large suggesting good plasticity. The

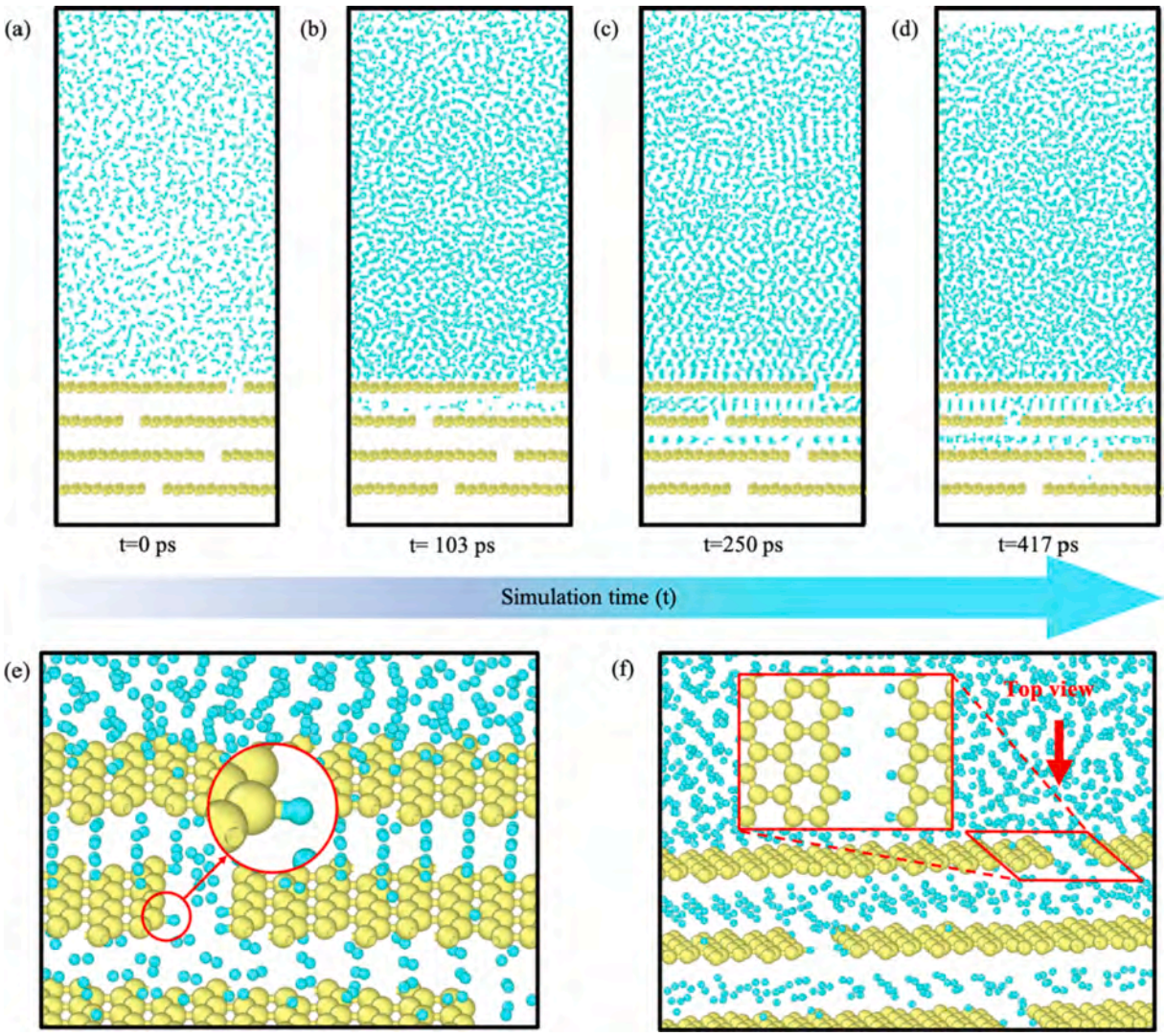

Fig. 9. Molecular dynamics simulation of the process in which hydrogen atoms penetrate the MLG: (a-d) Snapshots at selected time points and (e-f) Snapshots from the diffusion simulation for adsorption with the yellow and blue spheres representing carbon and hydrogen atoms, respectively. (For interpretation of the references to colour in this figure legend, the reader is referred to the web version of this article.)

dissociative fracture characteristics of hydrogen-induced fracture appear after hydrogen charging, revealing that hydrogen causes the transformation of the pipeline steel from plastic fracture to brittle fracture. However, the fracture of the sample coated with MLG coating after charging retains the dimple morphology similar to that of the pipeline steel without charging. Therefore, the MLG samples maintain good plasticity after long-term hydrogen charging and the MLG coating alleviates hydrogen embrittlement of the pipeline steel consistent with the tensile results.

3.3. Corrosion resistance

Electrochemical impedance spectroscopy (EIS) is performed to determine the corrosion behavior of the different samples in 3.5% NaCl at room temperature. As shown in Fig. 6(a), the Nyquist curves show capacitance semicircles with different diameters. The capacitance loops of the coated samples are obviously larger than those of the untreated samples and MLG further increases the diameter of the capacitance loop. The results show that the coating protects the substrate from corrosion. The Bode plots are shown in Fig. 6(b). The impedance moduli of the bare X70 steel, X70-MLG, and X70-Ni at a low frequency (0.1 Hz) are 452.2 Ω/cm^2, 4241 Ω/cm^2, and 3380 Ω/cm^2, respectively. The impedance modulus of the MLG coating is much large than that of the bare X70, implying that the coating isolates the substrate from the corrosive environment and so the blocking and shielding properties are improved.

The equivalent circuit models in Fig. 7 are employed to fit the EIS process. The $R_{soln}(Q_c[R_{cor}])$ model is used for the bare steel substrate and the $R_{soln}(Q_c[R_{po}(Q_{cor}[R_{cor}])])$ model is used for the coated samples. R_{soln} represents the solution resistance, Q_c indicates the constant phase element, R_{po} is the pore resistance, Q_{cor} and R_{cor} are the capacitance of the double-layer and polarization resistance, respectively. R_{po} and R_{cor} of the different samples are fitted as shown in Fig. 6(c). Compared to the bare steel, X70-Ni shows larger R_{por} and R_{cor}, furnishing evidence that the coating improves the corrosion resistance. R_{por} and R_{cor} increase further due to the MLG layer. A larger R_{por} reflects low porosity [39] and it can be inferred that the impermeable graphene reduces the porosity and the active area exposed to the corrosive environment.

Potentiodynamic polarization is performed to assess the corrosion properties as shown in Fig. 6(d). Table 3 summarizes the corrosion potentials (E_{cor}) and corrosion current densities (I_{cor}) derived from the Tafel curves. The higher the corrosion potential, the smaller is the corrosion tendency and the better is the corrosion resistance [40]. Meanwhile, the smaller the corrosion current density, the lower is the corrosion rate and the better the corrosion resistance. The pure Ni

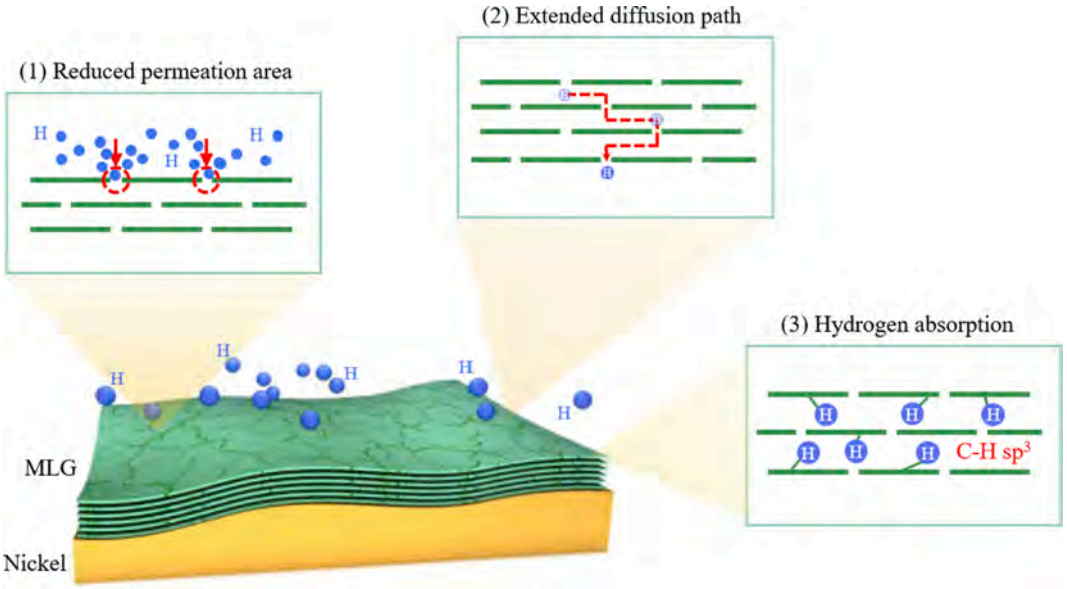

Fig. 10. Internal hydrogen resistance mechanism of the MLG coating.

coating shows $E_{cor} = -0.442$ V, which is higher than that of the X70 pipeline steel indicating better corrosion resistance. There is no significant difference between the corrosion potential of the MLG coating and that of the pure Ni coating. After fabricating MLG on the Ni surface, the corrosion current density shows a negative shift compared to the pure Ni coating confirming that the corrosion rate of MLG is the smallest. The results provide strong evidence that the MLG coating enhances the corrosion resistance.

3.4. Hydrogen resistance mechanism

3.4.1. Surface inhibition

Environmental corrosion of pipeline steel during service is frequently caused by hydrogen embrittlement of the materials and reduction of permeation and diffusion of hydrogen by means of surface coatings is a viable solution. [41,42] In the corrosion process, hydrogen is generated by the electrochemical hydrogen evolution reaction (HER) as follows:

$$H_2O + e^- \rightarrow H + OH^- \quad (3)$$

The hydrogen equilibrium potential of HER is calculated by Nernst Equation [43]:

$$E_e = E_e^0 + 0.0592\, log\,[H^+] = -0.0592\text{pH}, \quad (4)$$

where E_e is the hydrogen equilibrium potential, E_e^0 is the hydrogen standard equilibrium potential, and $[H^+]$ is the concentration of hydrogen ions in the solution. The potential of SCE relative to SHE is 0.2412 V (vs. SHE). When the concentration of OH^- is 0.2 mol/L, the equilibrium potential of HER is 1.029 V (vs. SCE). The cathodic polarization curve is displayed in Fig. 8. The hydrogen evolution potential E is obtained and then E_e is subtracted to obtain the hydrogen evolution overpotential η (Table 4) which reflects the difficulty of HER on the surface. The smaller is η, the easier is the hydrogen evolution. η of X70 is 0.146 V and the Ni coating changes η to 0.107 V, indicating that hydrogen evolution is more likely to occur on the Ni coating. After fabrication of MLG on the Ni layer, η increases to 0.455 V indicative of reduced activity and more difficult HER. The Tafel slope -b obtained from the cathodic polarization curve shows the rate of hydrogen evolution. The smaller the Tafel slope, the faster is the hydrogen evolution rate. The MLG sample shows the largest Tafel slope indicating that MLG inhibit HER and reduces the number of hydrogen atoms adsorbed on the sample surface, ultimately mitigating the risk of HE.

3.4.2. Internal barrier

Molecular dynamics simulation is performed to assess the diffusion process of hydrogen atoms in MLG. As shown in Fig. 9, the MLG model consists of four graphene monolayers with an interlayer spacing of 0.66 nm, which is equal to the size determined experimentally. 5000 hydrogen atoms with Brownian motion are randomly placed above the MLG and under a certain driving force, hydrogen atoms begin to diffuse downward.

Fig. 9(a-d) show the snapshots during diffusion of hydrogen atoms in MLG at different time. It is difficult for hydrogen atoms to pass through the defect free graphene sheet [14] and so they can only diffuse through the gap of the graphene boundary. Fig. 9(b) shows diffusion of hydrogen atoms to the first layer and Fig. 9(d) is that in the third layer. Hydrogen atoms diffuse downward layer-by-layer and the diffusion path is prolonged in this process. A small number of hydrogen atoms eventually pass through the fourth layer. In addition, there are some unsaturated dangling bonds in MLG. These bonds are employed in the graphene model to study their effects. As shown in Fig. 9(e-f), the C-H sp^3 bond is formed by combination of the graphene suspended bonds and hydrogen atoms to reflect adsorption of hydrogen atoms on graphene.

3.4.3. Hydrogen resistance mechanism

Hydrogen atoms adsorbing on the surface must overcome the internal barrier effects of the MLG coating before reaching the pipeline steel substrate and the mechanism is illustrated in Fig. 10. Firstly, the impermeability of defect free multi-layered graphene reduces the permeation area. The AB stacking (the hexagonal rings in each graphene layer are centred on the carbon atoms in the adjacent layer) of graphene results in 'pores' in the electron cloud of one layer being covered by electron density maxima within the adjacent layer. [15] Secondly, the *in situ* grown graphene layers are stacked and interpenetrated each other to provide good coverage. The stacked structure prolongs the diffusion path of hydrogen atoms and diffusion time. Thirdly, graphene has strong adsorption for hydrogen atoms to create hydrogen traps to capture hydrogen atoms. [14] The multilayered structure of graphene enhances hydrogen adsorption and capture. Graphene has been shown to be feasible hydrogen storage materials with limited storage capacity. [44] When hydrogen adsorption reaches saturation, hydrogen adsorption ceases and afterwards, permeation and diffusion of hydrogen are inhibited.

4. Conclusion

A multi-layered graphene (MLG) coating is prepared *in situ* on the X70 pipe steel by ion implantation and annealing. The graphene structure has layer-by-layer stacking and the layers interpenetrate each other. After annealing, carbon diffusion and the solid solution formed between the nickel coating and substrate improve the adhesion strength of the coating. The MLG coating has excellent hydrogen resistance as manifested by reduction of D_{app} by 123 times and J by 48 times. After hydrogen pre-charging, the mechanical properties of the samples coated with MLG do not change and so the susceptibility to HE decreases significantly. Electrochemical evaluation demonstrates that MLG coating improves the corrosion resistance. The enhancement of the hydrogen resistance property was related to the dual effects rendered by surface inhibition and the internal barrier. MLG reduces the amount of surface permeable hydrogen by inhibiting the process of hydrogen evolution. At the same time, MLG mitigates diffusion of hydrogen by extending the diffusion path, decreasing the permeation area, and enhancing hydrogen adsorption, consequently forming a protective barrier on the X70 steel. The results and theoretical investigation reveal not only the mechanisms, but also that it is a viable technique to improve the hydrogen resistance of commercial steels.

CRediT authorship contribution statement

Kejun Shi: Conceptualization, Methodology, Data curation, Writing – original draft, Writing – review & editing. **Shu Xiao:** Conceptualization, Methodology, Formal analysis, Writing – review & editing, Funding acquisition, Supervision. **Qingdong Ruan:** Resources, Data curation. **Hao Wu:** Investigation, Formal analysis, Validation, Project administration. **Guohua Chen:** Conceptualization, Supervision. **Chilou Zhou:** Methodology, Writing – original draft. **Saihua Jiang:** Methodology, Writing – original draft. **Ke Xi:** Data curation. **Mohan He:** Data curation. **Paul K. Chu:** Conceptualization, Writing – original draft.

Declaration of Competing Interest

The authors declare that they have no known competing financial interests or personal relationships that could have appeared to influence the work reported in this paper.

Acknowledgements

We acknowledge the financial support from National Natural Science Foundation of China (Nos. 52005187 and 51905177), Basic and Applied Basic Research Foundation of Guangdong Province (No. 2019A1515110065), Fundamental Research Funds for the Central Universities of China (No. 2019MS063), China Postdoctoral Science Foundation (No. 2019M662909), and City University of Hong Kong Strategic Research Grant (SRG) (No. 7005505).

References

[1] J.O. Abe, A.P.I. Popoola, E. Ajenifuja, O.M. Popoola, Hydrogen energy, economy and storage: Review and recommendation, Int. J. Hydrogen Energy 44 (29) (2019) 15072–15086.
[2] M. Deymi-Dashtebayaz, A. Ebrahimi-Moghadam, S.I. Pishbin, M. Pourramezan, Investigating the effect of hydrogen injection on natural gas thermo-physical properties with various compositions, Energy 167 (2019) 235–245.
[3] M. Dadfarnia, A. Nagao, S. Wang, M.L. Martin, B.P. Somerday, P. Sofronis, Recent advances on hydrogen embrittlement of structural materials, Int. J. Fract. 196 (1-2) (2015) 223–243.
[4] J.D. Fowler, D. Chandra, T.S. Elleman, A.W. Payne, K. Verghese, Tritium Diffusion in Al_2O_3 and BeO, J. Am. Ceram. Soc. 60 (3–4) (1977) 155–161.
[5] Z. Yao, A. Suzuki, D. Levchuk, T. Terai, SiC Coating by RF Sputtering as Tritium Permeation Barrier for Fusion Blanket, Fusion Sci. Technol. 52 (4) (2007) 865–869.
[6] T. Chikada, A. Suzuki, T. Terai, Deuterium permeation and thermal behaviors of amorphous silicon carbide coatings on steels, Fusion Eng. Des. 86 (9-11) (2011) 2192–2195.
[7] Q. Li, J. Wang, Q.-Y. Xiang, K. Yan, W.-Q. Yao, J.-L. Cao, Study on influence factors of permeation reduction factor of Al_2O_3-hydrogen isotopes permeation barriers, Int. J. Hydrogen Energy 41 (7) (2016) 4326–4331.
[8] D. Levchuk, S. Levchuk, H. Maier, H. Bolt, A. Suzuki, Erbium oxide as a new promising tritium permeation barrier, J. Nucl. Mater. 367-370 (2007) 1033–1037.
[9] Y. Wu, S. Zhu, T. Liu, F. Li, Y. Zhang, Y. Rao, Y. Zhang, Preparation and properties of erbium oxide films deposited by radio frequency magnetron sputtering, Appl. Surf. Sci. 307 (2014) 615–620.
[10] V. Berry, Impermeability of graphene and its applications, Carbon 62 (2013) 1–10.
[11] L.i. Liu, S. Ryu, M.R. Tomasik, E. Stolyarova, N. Jung, M.S. Hybertsen, M. L. Steigerwald, L.E. Brus, G.W. Flynn, Graphene oxidation: thickness-dependent etching and strong chemical doping, Nano Lett. 8 (7) (2008) 1965–1970.
[12] J.S. Bunch, S.S. Verbridge, J.S. Alden, A.M. van der Zande, J.M. Parpia, H. G. Craighead, P.L. McEuen, Impermeable Atomic Membranes from Graphene Sheets, Nano Lett. 8 (8) (2008) 2458–2462.
[13] O. Leenaerts, B. Partoens, F.M. Peeters, Graphene: A perfect nanoballoon, Appl. Phys. Lett. 93 (19) (2008) 193107, https://doi.org/10.1063/1.3021413.
[14] M. Miao, M.B. Nardelli, Q. Wang, Y. Liu, First principles study of the permeability of graphene to hydrogen atoms, PCCP 15 (38) (2013) 16132–16137.
[15] S. Hu, M. Lozada-Hidalgo, F.C. Wang, A. Mishchenko, F. Schedin, R.R. Nair, E. W. Hill, D.W. Boukhvalov, M.I. Katsnelson, R.A.W. Dryfe, I.V. Grigorieva, H.A. Wu, A.K. Geim, Proton transport through one-atom-thick crystals, Nature 516 (7530) (2014) 227–230.
[16] P.Z. Sun, Q. Yang, W.J. Kuang, Y.V. Stebunov, W.Q. Xiong, J. Yu, R.R. Nair, M. I. Katsnelson, S.J. Yuan, I.V. Grigorieva, M. Lozada-Hidalgo, F.C. Wang, A.K. Geim, Limits on gas impermeability of graphene, Nature 579 (7798) (2020) 229–232.
[17] M. Bartolomei, M.I. Hernández, J. Campos-Martínez, R. Hernández-Lamoneda, G. Giorgi, Permeation of chemisorbed hydrogen through graphene: A flipping mechanism elucidated, Carbon 178 (2021) 718–727.
[18] K.T. Young, C. Smith, T.M. Krentz, D.A. Hitchcock, E.M. Vogel, Graphene synthesized by chemical vapor deposition as a hydrogen isotope permeation barrier, Carbon 176 (2021) 106–117.
[19] T.-H. Nam, J.-H. Lee, S.-R. Choi, J.-B. Yoo, J.-G. Kim, Graphene coating as a protective barrier against hydrogen embrittlement, Int. J. Hydrogen Energy 39 (22) (2014) 11810–11817.
[20] Y. Fan, Y. Huang, B. Cui, Q. Zhou, Graphene coating on nickel as effective barriers against hydrogen embrittlement, Surf. Coat. Technol. 374 (2019) 610–616.
[21] X. Li, L. Colombo, R.S. Ruoff, Synthesis of Graphene Films on Copper Foils by Chemical Vapor Deposition, Adv. Mater. 28 (29) (2016) 6247–6252.
[22] S.-M. Kim, J.-H. Kim, K.-S. Kim, Y. Hwangbo, J.-H. Yoon, E.-K. Lee, J. Ryu, H.-J. Lee, S. Cho, S.-M. Lee, Synthesis of CVD-graphene on rapidly heated copper foils, Nanoscale 6 (9) (2014) 4728–4734.
[23] D.V. Nikolaev, V.I. Popov, V.B. Timofeev, S.A. Smagulova, Chemical Vapor Deposition Synthesis of Large-Area Graphene Films, J. Struct. Chem. 59 (4) (2018) 766–772.
[24] S.J. Chae, F. Günes, K.K. Kim, E.S. Kim, G.H. Han, S.M. Kim, H.-J. Shin, S.-M. Yoon, J.-Y. Choi, M.H. Park, C.W. Yang, D. Pribat, Y.H. Lee, Synthesis of Large-Area Graphene Layers on Poly-Nickel Substrate by Chemical Vapor Deposition: Wrinkle Formation, Adv. Mater. 21 (22) (2009) 2328–2333.
[25] J.H. Mun, S.K. Lim, B.J. Cho, Local Growth of Graphene by Ion Implantation of Carbon in a Nickel Thin Film followed by Rapid Thermal Annealing, J. Electrochem. Soc. 159 (6) (2012) G89–G92.
[26] L. Baraton, Z. He, C.S. Lee, J.-L. Maurice, C.S. Cojocaru, A.-F. Gourgues-Lorenzon, Y.H. Lee, D. Pribat, Synthesis of few-layered graphene by ion implantation of carbon in nickel thin films, Nanotechnology 22 (8) (2011) 085601, https://doi.org/10.1088/0957-4484/22/8/085601.
[27] P. Zhou, W. Li, X. Zhu, Y. Li, X. Jin, J. Chen, Graphene Containing Composite Coatings as a Protective Coatings against Hydrogen Embrittlement in Quenching & Partitioning High Strength Steel, J. Electrochem. Soc. 163 (5) (2016) D160–D166.
[28] K. Shi, X. Meng, S. Xiao, G. Chen, H. Wu, C. Zhou, S. Jiang, P. Chu, MXene coatings: novel hydrogen permeation barriers for pipe steels, Nanomaterials 11 (10) (2021) 2737.
[29] E. Martínez-Pañeda, Z.D. Harris, S. Fuentes-Alonso, J.R. Scully, J.T. Burns, On the suitability of slow strain rate tensile testing for assessing hydrogen embrittlement susceptibility, Corros. Sci. 163 (2020) 108291, https://doi.org/10.1016/j.corsci.2019.108291.
[30] S. Plimpton, Fast parallel algorithms for short-range molecular dynamics, J. Comput. Phys. 117 (1) (1995) 1–19.
[31] S.J. Stuart, A.B. Tutein, J.A. Harrison, A reactive potential for hydrocarbons with intermolecular interactions, J. Chem. Phys. 112 (14) (2000) 6472–6486.
[32] S.M. Kozlov, F. Viñes, A. Görling, Bonding Mechanisms of Graphene on Metal Surfaces, J. Phys. Chem. C 116 (13) (2012) 7360–7366.
[33] L. Baraton, Z.B. He, C.S. Lee, C.S. Cojocaru, M. Châtelet, J.-L. Maurice, Y.H. Lee, D. Pribat, On the mechanisms of precipitation of graphene on nickel thin films, EPL (Europhys. Lett.) 96 (4) (2011) 46003, https://doi.org/10.1209/0295-5075/96/46003.
[34] F. Ye, Q. Song, Z. Zhang, W. Li, S. Zhang, X. Yin, Y. Zhou, H. Tao, Y. Liu, L. Cheng, L. Zhang, H. Li, Direct growth of edge-rich graphene with tunable dielectric properties in porous Si_3N_4 ceramic for broadband high-performance microwave absorption, Adv. Funct. Mater. 28 (17) (2018) 1707205, https://doi.org/10.1002/adfm.v28.1710.1002/adfm.201707205.
[35] A. Ermolieff, A. Chabli, F. Pierre, G. Rolland, D. Rouchon, C. Vannuffel, C. Vergnaud, J. Baylet, M.N. Séméria, XPS, Raman spectroscopy, X-ray diffraction, specular X-ray reflectivity, transmission electron microscopy and elastic recoil detection analysis of emissive carbon film characterization, Surf. Interface Anal. 31 (3) (2001) 185–190.

[36] Y.i. Zhang, L. Gomez, F.N. Ishikawa, A. Madaria, K. Ryu, C. Wang, A. Badmaev, C. Zhou, Comparison of Graphene Growth on Single-Crystalline and Polycrystalline Ni by Chemical Vapor Deposition, J. Phys. Chem. Lett. 1 (20) (2010) 3101–3107.
[37] A. Turk, D. Bombač, J. Jelita Rydel, M. Zięta ra, P.E.J. Rivera-Díaz-del-Castillo, E. I. Galindo-Nava, Grain boundary carbides as hydrogen diffusion barrier in a Fe-Ni alloy: a thermal desorption and modelling study, Mater. Des. 160 (2018) 985–998.
[38] A. Oudriss, J. Creus, J. Bouhattate, E. Conforto, C. Berziou, C. Savall, X. Feaugas, Grain size and grain-boundary effects on diffusion and trapping of hydrogen in pure nickel, Acta Mater. 60 (19) (2012) 6814–6828.
[39] C. Liu, Q. Bi, A. Leyland, A. Matthews, An electrochemical impedance spectroscopy study of the corrosion behaviour of PVD coated steels in 0.5 N NaCl aqueous solution: Part II.: EIS interpretation of corrosion behaviour, Corros. Sci. 45 (6) (2003) 1257–1273.
[40] Y.u. Gao, Y. Zhou, D. Dai, N. Sun, H. Tan, Z. Zhan, J. Cai, X. Cai, Controllable preparations and anti-corrosion properties of reduced graphene oxide films by binder-free electrophoretic deposition, Appl. Surf. Sci. 563 (2021) 150295, https://doi.org/10.1016/j.apsusc.2021.150295.
[41] P. Zhou, W. Li, X. Jin, Comparison of Hydrogen Permeation Properties of Pure Ni, Ni-MoS_2, Ni-Graphene Composite Coatings Deposited on Quenching and Partitioning Steel and the Hot-Dipping Galvanized Steel, J. Electrochem. Soc. 164 (7) (2017) D394–D400.
[42] W. Ensinger, Ion-beam sputter coating of tantalum tube inner walls for protection against hydrogen embrittlement, Surf. Coat. Technol. 84 (1-3) (1996) 434–438.
[43] F. Ge, F. Huang, W. Yuan, Z. Peng, J. Liu, Y.F. Cheng, Effect of tensile stress on the hydrogen permeation of MS X65 pipeline steel under sulfide films, Int. J. Hydrogen Energy 45 (22) (2020) 12419–12431.
[44] V. Tozzini, V. Pellegrini, Prospects for hydrogen storage in graphene, PCCP 15 (1) (2013) 80–89.